Nr. 49
23. July 2018

universität innsbruck
Institut für Mathematik

Preprint-Series: Department of Mathematics - Applied Mathematics

Compressed Sensing for Multiple Excitation Magnetorelaxometry Imaging

M. Haltmeier, G. Zangerl, P. Schier, D. Baumgarten

APPLIEDMATHEMATICS

Technikerstraße 13 - 6020 Innsbruck - Austria
Tel.: +43 512 507 53803 Fax: +43 512 507 53898
https://applied-math.uibk.ac.at

Compressed Sensing for Multiple Excitation Magnetorelaxometry Imaging

MarkusHaltmeier[1,⋆], Gerhard Zangerl[1], Peter Schier[1], and Daniel Baumgarten[2]

[1]Department of Mathematics, University of Innsbruck
Technikerstraße 13, 6020 Innsbruck, Austria

[2]Institute of Electrical and Biomedical Engineering, Private University for Health Sciences, Medical Informatics and Technology (UMIT)
Eduard-Wallnöfer-Zentrum 1, A-6060 Hall in Tirol, Austria

[⋆]Correspondence: markus.haltmeier@uibk.ac.at

May 4, 2018

Abstract

Magnetorelaxometry imaging is a novel tool for quantitative determination of the spatial distribution of magnetic nanoparticles inside an organism. While the use of multiple excitation patterns has been demonstrated to significantly improve spatial resolution, the use of several activation patterns is considerably more time consuming as several experiments have to be performed in a sequential manner. In this paper, we use compressed sensing in combination with sparse recovery, for reducing scanning time while keeping improved spatial resolution. We investigate single-stage and two-stage approaches for image reconstructing and sparse recovery algorithms based on Douglas Rachford splitting. Our numerical experiments demonstrate that the single-stage approach clearly outperforms the two-stage approach. Further, the proposed single-stage algorithm is shown to be capable to recover the magnetic nanoparticles with high spatial resolution from a small number of activation patterns.

Keywords: Compressed sensing; magnetorelaxometry; image reconstruction; magnetic nanoparticles; multiple excitation; Douglas Rachford splitting; sparse recovery.

1 Introduction

Magnetic nanoparticles (MNP) offer a variety of promising biomedical applications. For example, they can be used as agents for drug delivery or hyperthermia, where the aim is to heat up specific regions inside a biological specimen [27]. These applications require quantitative knowledge of the magnetic nanoparticles distribution for safety and efficacy monitoring. In this paper, we consider magnetorelaxometry (MRX) imaging, which is a novel and promising non-invasive technique to spatially resolve the location and concentration of magnetic particles in vivo [4, 19], and beneficially combines a highly sensitive magnetic measurement technology for MNP imaging with a broad range of parameters and the potential to image particle distributions in a comparably large volume [9].

In MRX, the magnetic moments of the magnetic nanoparticles are aligned by a magnetic field generated by excitation coils [20]. Therewith, a magnetization can be measured from the MNP. After switching off the excitation field, the decay of magnetization (relaxation) is recorded, typically by SQUID sensors, yielding information about the particle concentration and other properties. If the relaxation is measured by a sensor array, the particle distribution can be reconstructed by inverse imaging methods [3, 19].

In multiple excitation MRX (ME-MRX), several inhomogeneous activation fields generated by an array of excitation coils are applied. With such a coil array, a variety of inhomogeneous excitation fields can be generated, for example, by switching on the coils in a sequential manner [24]. First experimental realization of ME-MRX with sequential activation and least squares estimation for imaging has been obtained in [19].

ME-MRX using sequential coil activation requires a large number of measurement cycles and thus a considerable time for data acquisition. Recently, different approaches have been proposed for advanced excitation schemes [7, 8, 1].

A possibility to maintain improved resolution while reducing measurement time is via compressed sensing (CS), a new sensing paradigm [5, 11] that allows to capture a high resolution image (or signal) by using much fewer measurements than predicted by Shannon's sampling theorem. CS replaces point-measurements by general linear measurements, where each measurement consists of a linear combination of the entries of the image of interest. Recovering the original image is highly under-determined. The standard theory of CS predicts that under suitable assumptions on the image of interest (sparsity) and the measurement matrix (incoherence), stable image reconstruction is nevertheless possible. CS has led to several new sampling strategies in medical imaging, for example, for speeding up MRI data acquisition [21], accelerating photoacoustic tomography [17], or completing under-sampled CT images [6]. While these applications involve relatively mildly ill-conditioned problems, ME-MRX constitutes a severely ill-conditioned or ill-posed problem. No standard approaches for image reconstruction combining compressive measurements and such severely ill-posed problems exist.

In this work, we investigate CS techniques for accelerating ME-MRX. For that purpose, we consider random activations of the coils as well as sparse deterministic subsampling schemes. For reconstructing the magnetic particle distribution from the CS data we develop two-stage and single-stage reconstruction approaches. In the two-stage approach, the CS data are used to recover the complete data (corresponding to a full sequential activation pattern) in a first step, from which the magnetic particle distribution is recovered in a second stage. In the single-stage approach, the magnetic particle distribution is directly recovered from the CS data. For both approaches, we develop sparse reconstruction algorithms based on Douglas Rachford splitting [10]. Note that due to the ill-posed nature of the MRX inverse problem, the standard uniform CS recovery theory [13] cannot be applied to the single-stage approach. Nevertheless, our numerical results demonstrate that the single-stage approach works well, and significantly outperforms the two-stage approach in terms of reconstruction quality. We therefore recommend the single-stage approach for further investigations in CS ME-MRX imaging.

1.1 Outline

This article is organized as follows. In Section 2 we describe the forward problem of ME-MRX imaging and CS. The proposed single-stage and two-stage algorithms for ME-MRX image reconstruction are developed in Section 3. Details on the numerical implementation together with numerical results and a discussion are presented in Section 4. The paper ends with a conclusion

and outlook presented in Section 4.

2 The forward model in ME-MRX imaging

This section gives a precise formulation of the forward problem of ME-MRX and CS. For the sake of clarity, throughout we work with a discrete model [26, 4, 22]. A continuous model has recently been presented in [12].

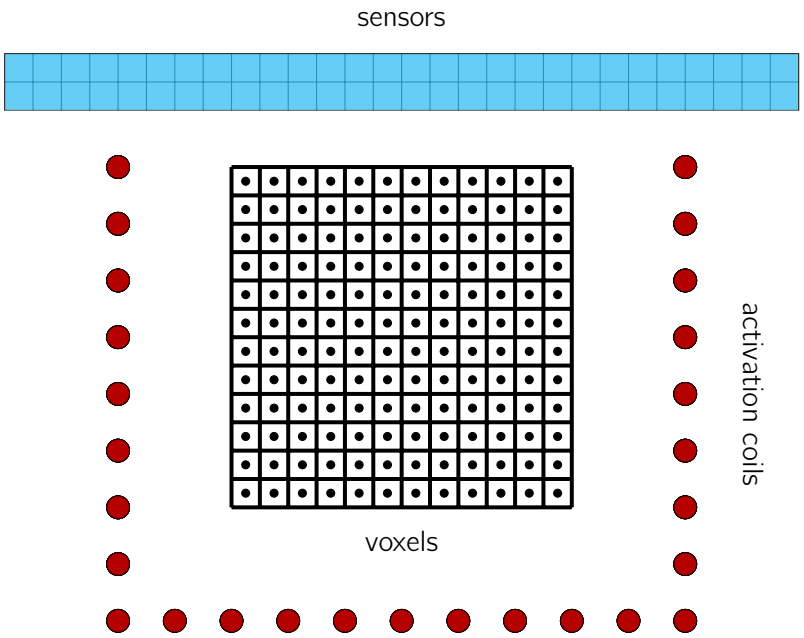

Figure 1: Illustration of a simplified two-dimensional ME-MRX setup consisting of an array of activation coils (each having location $\mathbf{r}_s$ and normal vector $\boldsymbol{\nu}_s$) and two layers of sensors arranged around the volume of interest.

2.1 Signal generation

In MRX, an activation field is applied to a region of interest containing magnetic particles. We assume this region to be divided into a number of N_v quadratic voxels, each represented by its midpoint located at $\mathbf{r}_v$ and containing a concentration of magnetic particles $n(\mathbf{r}_v)$ (compare Fig. 1). Due to the presence of the applied field, the magnetic particles align up and, after the activation field is switched off, produce a relaxation signal. According to Biot-Savart law, the contribution of the magnetic particles concentration in the vth voxel to the measured signal at sensor location $\mathbf{r}_s$ is given by [19]

$$b^{\mathrm{H}}(\mathbf{r}_s) = \frac{\mu_0}{4\pi}\,\boldsymbol{\nu}_s \bullet \sum_{v=1}^{N_v} \left(\frac{3\mathbf{r}_{s,v} \otimes \mathbf{r}_{s,v}}{|\mathbf{r}_{s,v}|^5} - \frac{1}{|\mathbf{r}_{s,v}|^3} \right) \mathbf{H}(\mathbf{r}_v)\, n(\mathbf{r}_v) \quad \text{for } s \in \{1, \ldots, N_s\}\,. \tag{1}$$

Here $\mathbf{H}$ is the activation field, $\mathbf{r}_{s,v} = \mathbf{r}_s - \mathbf{r}_v$ is the vector joining $\mathbf{r}_s$ and $\mathbf{r}_v$, $\boldsymbol{\nu}_s$ is the normal vector of the sensor at location $\mathbf{r}_s$, and $\otimes$ and $\bullet$ are used to denote the tensor and scalar product, respectively.

Assuming the concentrations $n(\mathbf{r}_v)$ and the activation field $\mathbf{H}$ to be known, the measured data can be computed by (1). Collecting the individual measurements in a vector $\mathbf{b}^{\mathsf{H}} = (b^{\mathsf{H}}(\mathbf{r}_1), \dots, b^{\mathsf{H}}(\mathbf{r}_{N_s}))^{\mathsf{T}}$, we obtain the linear equation

$$\mathbf{b}^{\mathsf{H}} = \mathcal{L}^{\mathsf{H}}\,\mathbf{n} \in \mathbb{R}^{N_s}\,. \tag{2}$$

Here $\mathbf{n} = (n(\mathbf{r}_1), \dots, n(\mathbf{r}_{N_v}))^{\mathsf{T}} \in \mathbb{R}^{N_v}$ is the vector of magnetic particle concentrations, and $\mathcal{L} \in \mathbb{R}^{N_s \times N_v}$ is the system matrix having entries

$$\mathcal{L}^{\mathsf{H}}_{s,v} \triangleq \frac{\mu_0}{4\pi}\,\boldsymbol{\nu}_s \bullet \left(\frac{3\mathbf{r}_{s,v} \otimes \mathbf{r}_{s,v}}{|\mathbf{r}_{s,v}|^5} - \frac{1}{|\mathbf{r}_{s,v}|^3}\right)\mathbf{H}(\mathbf{r}_v) \tag{3}$$

as derived from relation (1). The matrix $\mathcal{L}^{\mathsf{H}}$ is called Lead field matrix corresponding to the excitation field $\mathbf{H}$. Eq. (2) constitutes the standard discrete forward model of MRX using a single activation field.

2.2 Full coil activation

In ME-MRX, the volume of interest is (partially) surrounded by an array of excitation coils and sensor arrays (see Fig. 1). The coils can be controlled to generate different types of activation fields. In the following we denote by $\mathbf{H}_1, \dots, \mathbf{H}_{N_c}$ the magnetic fields induced by individual activation of the coils. Further, we write $\mathbf{b}_c \triangleq \mathbf{b}^{\mathsf{H}_c} \in \mathbb{R}^{N_s}$ and $\mathcal{L}_c \triangleq \mathcal{L}_{\mathsf{H}_c} \in \mathbb{R}^{N_s \times N_v}$ for the data and the Lead field matrix according to (2) and (3), corresponding to the activation field $\mathbf{H} = \mathbf{H}_c$. The measurements from all activations can be combined to a single equation of the form

$$\mathbf{b} = \mathcal{L}\,\mathbf{n} \in \mathbb{R}^{N_c N_s}\,, \tag{4}$$

where

$$\mathbf{b} \triangleq \begin{bmatrix} \mathbf{b}_1 \\ \vdots \\ \mathbf{b}_{N_c} \end{bmatrix} \quad \text{and} \quad \mathcal{L} \triangleq \begin{bmatrix} \mathcal{L}_1 \\ \vdots \\ \mathcal{L}_{N_c} \end{bmatrix}\,. \tag{5}$$

We will refer to $\mathbf{b}$ in (4) as full activation data. Evaluating (4) constitutes the forward model of ME-MRX. The corresponding inverse problem consists in determining the magnetic particle distribution $\mathbf{n} \in \mathbb{R}^{N_v}$ from the data vector $\mathbf{b}$ that is additionally corrupted by noise. Note that Eq. (4) is known to be severely ill-conditioned as its singular values are rapidly decreasing (see [2]; an analysis in the infinite-dimensional setting has been done in [12]).

The multiple coil setup has been been realized in [1, 24]. In order to collect the required data, any coil is switched on individually and data are collected by the sensor array. This process is repeated in a sequential manner until each coil in the array has been activated. The use of multiple excitation patters has been shown to significantly improve the spatial resolution compared to single activation [24]. However, the consecutive activation leads to a more time consuming measurement process. In order to accelerate data acquisition while keeping the advantages of multiple activation coils, in this paper we use CS techniques where we use random as well as deterministic coil activation patterns. Additionally, we develop sparse reconstruction algorithms for the arising CS ME-MRX inverse problems.

2.3 Compressive coil activations

The basic idea of employing CS for ME-MRX is to use m specific coil activations with $m \ll N_c$ instead of activating all N_c coils in a sequential manner. See Fig. 2 for a possible random activation

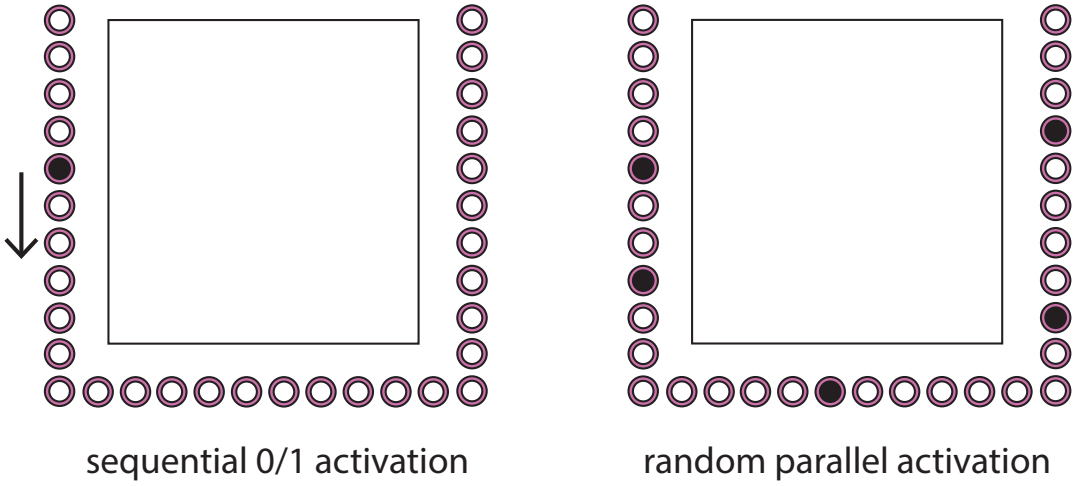

Figure 2: **Sequential versus random activation.** Left: Sequential activation, where the coils are turned on in an sequential manner. Right: A single random activation where several coils are turned on in a random manner.

pattern compared to sequential activation. Because of linearity, the data corresponding to the jth random activation pattern is given by

$$\mathbf{y}_j = \sum_{c=1}^{N_c} a_{j,c} b(\mathbf{r}_c) = \sum_{c=1}^{N_c} a_{j,c} (\mathcal{L}\mathbf{n})_c + \boldsymbol{\xi}_j \quad \text{for } j = 1, \ldots, m\,. \tag{6}$$

Here $\boldsymbol{\xi}_j$ models the error in the data and $a_{j,c}$ is the contribution of coil N_c to the jth activation pattern. The measurement matrix

$$\mathbf{A} \triangleq \begin{pmatrix} a_{1,1} & \cdots & a_{1,N_c} \\ \vdots & & \vdots \\ a_{m,1} & \cdots & a_{m,N_c} \end{pmatrix} \in \mathbb{R}^{m \times N_c} \tag{7}$$

represents all activation patters. Typical choices for $\mathbf{A}$ are Bernoulli or Gaussian matrices, since they are known to guarantee stable recovery of sparse signals [13]. Such kind of measurements can be realized in natural manner in ME-MRX, by simultaneous activation of several coils. The corresponding image reconstruction problem consists in recovering the magnetic particle distribution $\mathbf{n}$ from the data in (6).

2.4 Matrix formulation of the reconstruction problem

In order to write the reconstruction problem in a compact form we introduce some additional notation. First, we define the CS measurement vector as

$$\mathbf{y} \triangleq \begin{bmatrix} \mathbf{y}_1 \\ \vdots \\ \mathbf{y}_m \end{bmatrix} \in \mathbb{R}^{mN_s}\,. \tag{8}$$

Second, we introduce the vectorization or reshaping operator vec_{N_c}, that takes a matrix to a vector whose block entries are equal to the transposes of the rows of the matrix:

$$\mathrm{vec}_{N_c} : \mathbb{R}^{N_c \times N_s} \to \mathbb{R}^{N_c N_s} : \mathbf{X} \mapsto \begin{bmatrix} \mathbf{X}_{1,-}^{\mathsf{T}} \\ \vdots \\ \mathbf{X}_{N_c,-}^{\mathsf{T}} \end{bmatrix}\,. \tag{9}$$

We denote by mat_{N_c} the inverse reshaping operation that maps a vector in $\mathbb{R}^{N_c N_s}$ to a matrix in $\mathbb{R}^{N_c \times N_s}$. Further, we write $\mathbf{Y} \triangleq \mathrm{mat}_m \mathbf{y}$ and $\mathbf{B} \triangleq \mathrm{mat}_{N_c} \mathbf{b}$.

With the above notations, the CS data in (6) can be written in the compact form

$$\mathbf{Y} = \mathbf{A}\,\mathbf{L}\,\mathbf{n} + \Xi \in \mathbb{R}^{m \times N_s}\,, \tag{10}$$

where $\mathbf{L}$ is the reshaped Lead field matrix defined by the property $\mathbf{Ln} = \mathrm{mat}_{N_c}(\mathcal{L}\mathbf{n})$. With the Kronecker (or tensor) product $\mathcal{A} \triangleq \mathbf{A} \otimes \mathcal{I} \in \mathbb{R}^{(mN_s)\times(N_c N_s)}$ between the CS activation matrix $\mathbf{A}$ and the identity matrix $\mathcal{I} \in \mathbb{R}^{N_s \times N_s}$, equation (10) can further be rewritten in the form

$$\mathbf{y} = \mathcal{A}\,\mathcal{L}\,\mathbf{n} + \boldsymbol{\xi} \in \mathbb{R}^{mN_s}\,. \tag{11}$$

The image reconstruction task in CS ME-MRX now consists in recovering the magnetic particle distribution $\mathbf{n}$ from equation (10) or, equivalently, from equation (11).

3 Sparse reconstruction algorithms for CS ME-MRX imaging

In order to recover the magnetic particle distribution $\mathbf{n}$ from equation (10) (or (11)) we devise new sparse recovery algorithms. These methods will either follow a two-stage or a single-stage strategy. In the two-stage approach, the full measurement data $\mathbf{b}$ is recovered from the CS data as an intermediate result, from which the magnetic particle distribution is recovered in the second step. In the single-stage approach, the magnetic particle distribution is directly recovered from the CS data (11). We note that no standard approach for image reconstruction combining compressive measurements and severely ill-posed problems exist. This section is therefore also of interest from a general perspective on CS in inverse problems.

3.1 Single-stage reconstruction

Probably the most straightforward way to address CS ME-MRX is to view (11) as a single inverse problem with system matrix $\mathcal{M} = \mathcal{A}\mathcal{L}$. To address instability and non-uniqueness and to account for prior knowledge, we approach this by sparse regularization. For that purpose we minimize the generalized Tikhonov functional [23]

$$\mathcal{T}^{\mathcal{M}}_{\alpha,\beta}(\mathbf{n}) \triangleq \frac{1}{2}\|\mathbf{y} - \mathcal{M}\mathbf{n}\|_2^2 + \alpha\|\Psi\mathbf{n}\|_1 + \beta\mathcal{R}(\mathbf{n})\,. \tag{12}$$

Here $\Psi\colon \mathbb{R}^{N_v} \to \mathbb{R}^d$ is a transform that sparsifies the magnetic particle concentration, $\mathcal{R}\colon \mathbb{R}^{N_v} \to [0,\infty)$ is an additional regularizer that incorporates further a priori knowledge about the magnetic particle distribution (such as positivity and other convex constraints), and $\|\cdot\|_p$ is the standard ℓ^p-norm defined by

$$\|\mathbf{x}\|_p \triangleq \sqrt[p]{\sum_{i=1}^{d} |x_i|^p} \quad \text{for } \mathbf{x} = (x_1, \ldots, x_d) \in \mathbb{R}^d\,.$$

We call Ψ a sparsifying transform if $\Psi\mathbf{n}$ can well be approximated by k-sparse vectors $\mathbf{x}$, defined by the property that $\{i \mid x_i \neq 0\}$ has at most k elements.

Remark 1 (Recovery theory for (12))**.** *The s-RIP constant of $\mathcal{M} = \mathcal{A}\mathcal{L}$ (after appropriate scaling) is defined as the smallest number δ_k such that for all s-sparse vectors $\Psi\mathbf{n}$ we have*

$$(1-\delta_k)\|\mathbf{n}\|_2^2 \leq \|\mathcal{M}\mathbf{n}\|_2^2 \leq (1+\delta_k)\|\mathbf{n}\|_2^2\,. \tag{13}$$

Roughly spoken, standard CS theory [5, 13] predicts uniform stable recovery with (12) *(using* $\beta = 0$ *and orthogonal* Ψ*), in the sense that it stably recovers any s-sparse vector provided that the s-RIP constant of* $\mathcal{M}$ *is sufficiently small. Due to the severe ill-posedness of* $\mathcal{L}$*, the s-RIP is expected to be at most satisfied for very small problem size. Anyway, even in the case of full measurement data, where* $\mathcal{A}$ *is the identity matrix, uniform reconstruction seems hardly possible. To obtain quantitative error estimates for* (12)*, the stable recovery results for individual elements [14, 15, 16] are a promising alternative. Such theoretical investigations are beyond the scope of this paper and an interesting line of future research.*

In order to minimize (12), we propose using the Douglas Rachford minimization algorithm, which is an backward-backward type splitting method for minimizing the sum of two functionals F and G. For our purpose we take

$$F(\mathbf{n}) \triangleq \frac{1}{2}\|\mathbf{y} - \mathcal{M}\mathbf{n}\|_2^2 \tag{14}$$

$$G(\mathbf{n}) \triangleq \alpha\|\Psi\mathbf{n}\|_1 + \beta\mathcal{R}(\mathbf{n})\,. \tag{15}$$

The Douglas Rachford algorithm for minimizing (12) generates a sequence $(\mathbf{n}_k)_{k\in\mathbb{N}}$ of estimated magnetic particle distributions and auxiliary sequences $(\mathbf{z}_k)_{k\in\mathbb{N}}$, $(\tilde{\mathbf{z}}_k)_{k\in\mathbb{N}}$ as described in Algorithm 1.

Algorithm 1 Proposed single-stage reconstruction sparse recovery algorithm for CS ME-MRX.

1: Select $s \in (0, 2)$, and $\mu > 0$
2: Initialize $\mathbf{z}_0 = 0$
3: **for** $k = 1, \ldots, N_{\text{iter}}$ **do**
4: $\quad \mathbf{n}_k \leftarrow (\mathcal{M}^{\mathsf{T}}\mathcal{M} + \mu\mathcal{I})^{-1}(\mathcal{M}^{\mathsf{T}}\mathbf{y} + \mu\mathbf{z}_k)$
5: $\quad \tilde{\mathbf{z}}_k \leftarrow \operatorname{argmin}_{\tilde{\mathbf{z}}} \frac{\mu}{2}\|(2\mathbf{n}_k - \mathbf{z}_k) - \tilde{\mathbf{z}}\|_2^2 + G(\tilde{\mathbf{z}})$
6: $\quad \mathbf{z}_{k+1} \leftarrow \mathbf{z}_k + s(\tilde{\mathbf{z}}_k - \mathbf{n}_k)$
7: **end for**

Under the reasonable assumptions that the regularizer G is lower semicontinuous and convex, and that the sparse Tikhonov functional $\mathcal{T}_{\alpha,\beta}^{\mathcal{M}}$ is coercive, the sequence $(\mathbf{n}_k)_{k\in\mathbb{N}}$ generated by Algorithm 1 is known to converge to a minimizer of (12); see [10, 25]. Note that Algorithm 1 performs implicit steps with respect to the residual functional F, which we found to have much faster convergence than forward-backward type splitting algorithms that suffer from the ill-conditioned nature of $\mathcal{M}$.

For our numerical experiments we take $\Psi = \nabla$ as the discrete gradient operator as appropriate sparsifying transform for piecewise smooth magnetic particle distributions. The additional regularizer is taken as the indicator function $\mathcal{R} = I_C$ of the convex set

$$C \triangleq \{\mathbf{n} \mid \forall v\colon 0 \le n(v) \le n_{\max}\} \quad \text{for some bound } n_{\max}\,,$$

defined by $I_C(\mathbf{n}) = 0$ if $\mathbf{n} \in C$ and $I_C(\mathbf{n}) = \infty$. It guarantees non-negativity and boundedness, and (13) reduces to total variation regularization with box constraints. The minimization of $\frac{\mu}{2}\|\mathbf{n}-\mathbf{z}\|_2^2 + \|\nabla\mathbf{z}\|_1 + i_C(\mathbf{z})$ required for implementing Algorithm 1, is again performed by Douglas Rachford splitting.

3.2 Two stage reconstruction approach

An alternative reconstruction approach is based on a two-stage procedure. Thereby, the CS measurements are used to first recover the full activation data from which the magnetic particle

distribution is recovered in a second step. In order to recover the full activation data, note that the columns of $\mathbf{B}$, corresponding to CS data collected by individual sensors, satisfy

$$\mathbf{Y}_{-,s} = \mathbf{A}\mathbf{B}_{-,s} \ + \Xi_{-,s} \in \mathbb{R}^m \ \text{ for } s = 1, \dots N_s \,. \tag{16}$$

Eq. (16) is a family of N_s separate reconstruction problems involving the same measurement matrix $\mathbf{A}$, and known as the multiple measurement problem in the CS literature. In order to solve (16), we use sparse recovery. We determine an approximation to $\mathbf{B}$ by minimizing

$$\mathcal{T}^{\mathsf{A}}_{a,b}(\mathbf{B}) \triangleq \frac{1}{2}\|\mathbf{Y} - \mathbf{A}\mathbf{B}\|_{\mathsf{F}}^2 + a\|\Psi\mathbf{B}\|_1 + \frac{b}{2}\|\mathbf{D}\mathbf{B}\|_{\mathsf{F}}^2 \,, \tag{17}$$

where we $\|\cdot\|_{\mathsf{F}}$ is the Frobenius norm, Ψ is a sparsifying transform for $\mathbf{B}$ defined by an orthogonal basis $(\boldsymbol{\psi}_i)_i$, and $\mathbf{D}$ the second derivative with respect to the coil variable. The additional regularization term $(b/2)\,\|\mathbf{D}\mathbf{B}\|_{\mathsf{F}}^2$ accounts for the fact that the forward operator is smoothing and therefore $\mathbf{B}$ is expected to be smooth.

The functional (17) is again approached by Douglas Rachford splitting. The resulting algorithm is summarized in Algorithm 2, where $\mathrm{soft}_\mu(\,\cdot\,)$ denotes the soft-thresholding operation in the basis Ψ,

$$\mathrm{soft}_\mu(\mathbf{B}) \triangleq \sum_i \mathrm{sign}(\boldsymbol{\psi}_i \bullet \mathbf{B})\max\{|\boldsymbol{\psi}_i \bullet \mathbf{B}| - \mu), 0\}\,\boldsymbol{\psi}_i \,.$$

Because the sparse Tikhonov functional $\mathcal{T}^{\mathsf{A}}_{a,b}$ defined in (17) is coercive, the sequence $(\mathbf{B}_k)_{k\in\mathbb{N}}$ generated by Algorithm 2 converges to a minimizer of the $\mathcal{T}^{\mathsf{A}}_{a,b}$.

Algorithm 2 Proposed sparse data recovery algorithm for CS ME-MRX.

1: Select $s \in (0, 2)$, and $\mu > 0$
2: Initialize $\mathbf{Z}_0 = 0$
3: **for** $k = 1, \dots, N_{\text{iter}}$ **do**
4: $\quad \mathbf{B}_k \leftarrow (\mathbf{A}^{\mathsf{T}}\mathbf{A} + b\mathbf{D}^{\mathsf{T}}\mathbf{D} + \mu\mathbf{I})^{-1}(\mathbf{A}^{\mathsf{T}}\mathbf{Y} + \mu\mathbf{Z}_k)$
5: $\quad \mathbf{Z}_{k+1} \leftarrow \mathbf{Z}_k + s \cdot (\mathrm{soft}_\mu(2\mathbf{B}_k - \mathbf{Z}_k) - \mathbf{B}_k)$
6: **end for**

Having recovered an approximation of the complete data $\mathbf{B}$ by Algorithm 2, the magnetic particle distribution can be recovered by solving the full measurement data problem. For that purpose we use Algorithm 1 with $\mathcal{M} = \mathcal{L}$.

4 Numerical results

For the following numerical simulations, we use a data setup similar to the realization in [1]. For simplification, we consider a two-dimensional setup representing one voxel plane, containing two parallel arrays of detector elements (one measuring the horizontal $(1, 0)$ and one measuring the vertical $(0, 1)$ component) located outside a quadratic region of interest. Circular shaped activation coils are arranged in U-form around the region of interest all having the same normal vector $(0, 1)$. The used arrangement of sensor and coil locations for the full measurement data setup is shown in Fig. 3. For our simulations we choose a discretization of imaging space into $N_v = 75^2$ voxels covering a the region of interest of $[-5, 5] \times [-5, 5]$ cm^2. The data are generated for $N_s = 110$ positions and full measurement data corresponds to $N_c = 120$ activation coils outside region of interest.

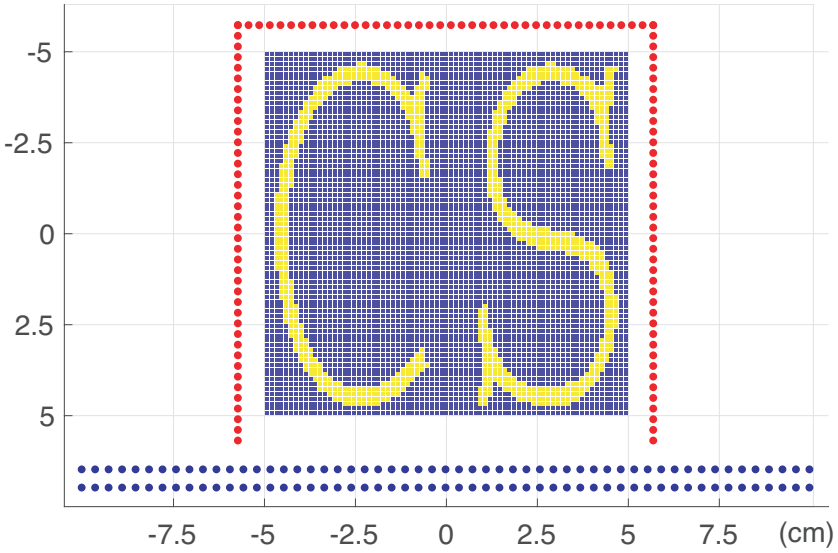

Figure 3: **Full data setup for the numerical simulations.** The phantom is contained in a square region of interest, the sensors are arranged in two parallel layers (blue dots), and the coils for full activation are arranged around the phantom in U-form (red dots).

4.1 Forward computations

To set up the forward model (2), (4), (5), we first have to compute the magnetic fields generated by each coil. For that purpose we follow the approach of [3, 1], where any circular activation coil is approximated by $n-1$ short line segments, each having the same current I_0. Using this approximation, the induced magnetic field at the voxel center $\mathbf{r}_v$ can be computed by (see [18])

$$\mathbf{H}(\mathbf{r}_v) \simeq \sum_{i=1}^{n-1} \frac{|\mathbf{r}_{1,v,i}| + |\mathbf{r}_{2,v,i}|}{|\mathbf{r}_{1,v,i}|\,|\mathbf{r}_{2,v,i}|} \cdot \frac{\mathbf{r}_{1,v,i} \times \mathbf{r}_{2,v,i}}{|\mathbf{r}_{1,v,i}|\,|\mathbf{r}_{2,v,i}| + \mathbf{r}_{1,v,i} \bullet \mathbf{r}_{2,v,i}} \, I_0 \,, \tag{18}$$

where $\mathbf{r}_{1,v,i}$ and $\mathbf{r}_{2,v,i}$ are the distance vectors between the voxel center $\mathbf{r}_v$ and the beginning and end points of the ith line segment, respectively. For the presented numerical computations we use $n-1 = 45$ line segments with a diameter of $1\,\bar{}\mathrm{m}$, illustrating an almost point like coil. Having computed the activation field $\mathbf{H}(\mathbf{r}_v)$, we compute the entries of the lead field matrix according to (2). By activating the coils sequentially, we obtain the full measurement data Lead field matrix.

For the presented results we use three different magnetic particle distributions which, together with the corresponding measurements full data, are shown in Fig. 4. Any column in the measurement data (in Fig. 4 and below) corresponds to a single activation pattern and contains the data of all detectors. The phantoms are rescaled to have maximum value 1 and the forward operator $\mathcal{L}$ is rescaled to have matrix norm $\|\mathcal{L}\|_2 = 1$. To all data we have added additive Gaussian noise amounting to an SNR of 80 dB. The corresponding reconstruction $(\mathcal{L}^{\mathsf{T}}\mathcal{L} + \mu\mathcal{I})^{-1}(\mathcal{L}^{\mathsf{T}}\mathbf{y} + \mu\mathbf{b})$ with standard quadratic Tikhonov regularization (penalized least squares) using regularization parameter $\mu = 10^{-12}$ are shown in the bottom row of Fig. 4. They can be seen as benchmark for the more sophisticated CS reconstructions applied to less data presented below.

The CS forward matrix $\mathcal{M} = \mathcal{A}\mathcal{L}$ is computed by multiplying the full Lead field matrix with $\mathcal{A}$. CS measurements have been generated in two random ways and one deterministic way. In the random case, $\mathbf{A}$ is taken either as Bernoulli matrix having entries ± 1 with equal probability, or a Gaussian matrix consisting of i.i.d. $\mathcal{N}(0,1)$-Gaussian random variables in each entry. The

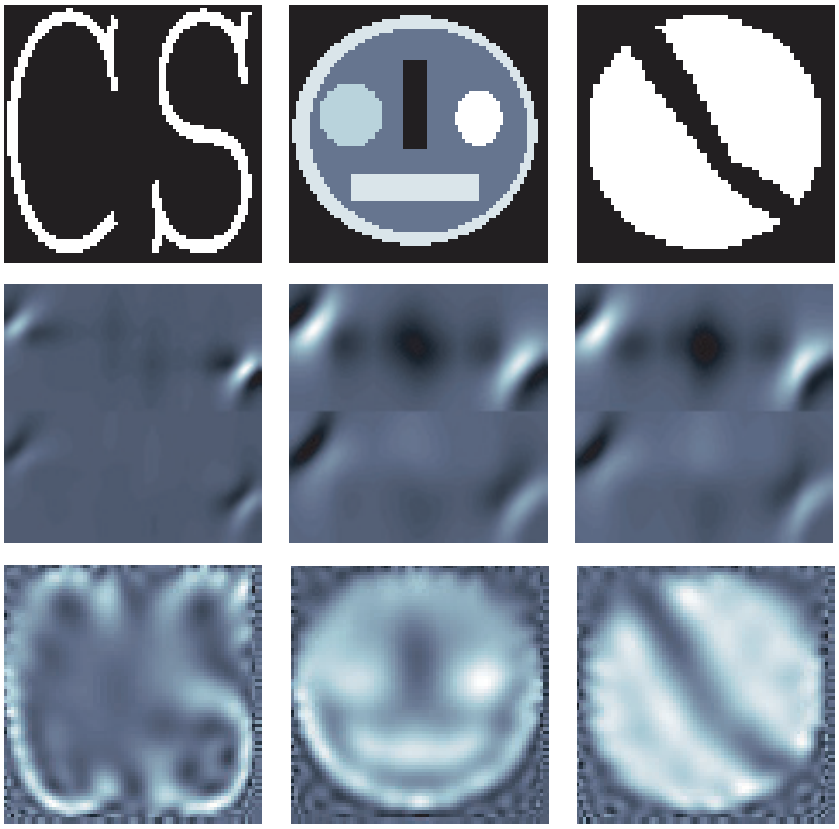

Figure 4: **Phantoms, data and full measurement data reconstruction.** Top row: CS-phantom (left), Smiley-phantom (middle) and tumor-phantom mimicking cancerous tissue with included blood vessel (right). Middle row: Corresponding full measurement data. Bottom row: Reconstructions from full measurement data using standard quadratic Tikhonov regularization.

deterministic subsampling is performed by choosing m equispaced coil activations. The CS data $\mathbf{B} = \mathbf{ALn}$ for $m = 40$ coil activations using the three sampling schemes and the three phantoms are shown in Fig. 5.

4.2 Results for the two-stage approach

In the two-stage reconstruction approach, the complete data $\mathbf{B}$ are recovered with Algorithm 2 in the first step. The results are shown in Fig. 6. We see that any data set is recovered well from the CS data. For the sparsifying transform Ψ we use the wavelet basis derived from Daubechies least asymmetric wavelet having 8 vanishing moments. The parameters are selected as $a = 10^{-8}$, $b = 10^{-10}$ in the regularization functional, and $s = 1$, $\mu = 10^{-8}$, $N_{\text{iter}} = 25$ for the numerical minimization. The relative mean squared errors $\|\mathbf{B} - \mathbf{B}^{\text{rec}}\|_{\text{F}}/\|\mathbf{B}\|_{\text{F}}$ are $(0.071, 0.063, 0.052)$ for the CS-phantom, $(0.046, 0.042, 0.046)$ for the Smiley-phantom and $(0.048, 0.046, 0.022)$ for the tumor-phantom. In particular, for the CS-phantom and the tumor-phantom the error is smallest for the deterministic subsampling scheme, whereas for the Smiley-phantom, the Bernoulli measurements lead to the smallest error.

Using the completed data from the first step, we recover the magnetic particle distribution using the proposed Algorithm 1 with $\mathcal{M} = \mathcal{L}$. The results of the two-stage procedure are

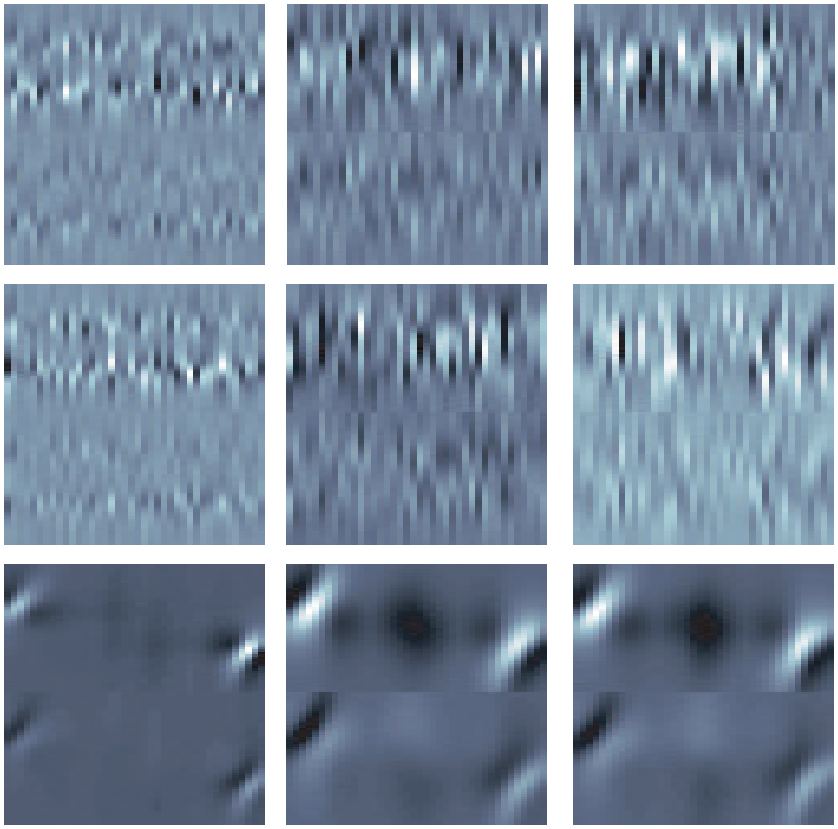

Figure 5: **Simulated CS data.** Top row: Gaussian activation matrix. Middle row: Bernoulli activation matrix. Bottom row: Deterministic activation. The data corresponds to the phantoms shown in Fig. 4 in the same order from left to right.

shown in Fig. 7. We used $\mu = \lambda = 5 \cdot 10^{-7}$, $s = 1$, $n_{\text{max}} = 1$ and $N_{\text{iter}} = 50$. The relative mean squared errors for the reconstructed particle distributions are $(0.88, 0.88, 0.85)$ for the CS-phantom, $(0.53, 0.52, 0.47)$ for the Smiley-phantom and $(0.35, 0.36, 0.32)$ for the tumor-phantom.

4.3 Results for the single-stage approach

In the single-stage approach, the phantoms are directly recovered from the CS data using the proposed Algorithm 1. We have rescaled $\mathcal{M}$ to have unit matrix norm and use the same parameter setting $\mu = 4 \cdot 10^{-13}$, $\lambda = 10^{-14}$, $s = 1$, $n_{\text{max}} = 1$ and $N_{\text{iter}} = 50$. The reconstructed magnetic particle distributions using the single-stage procedure from 40 coil activations are shown in Fig. 8. Each reconstruction with Algorithm 1 takes about 50 seconds in Matlab R 2017a on a MacBook Pro (2016) with 2.9 GHz Intel Core i7 processor. The relative mean squared errors are $(0.41, 0.42, 0.38)$ for the CS-phantom, $(0.34, 0.34, 0.30)$ for the Smiley-phantom and $(0.14, 0.14, 0.14)$ for the tumor-phantom. These numbers as well as visual inspection show that the single-stage approach significantly outperforms the two-stage procedure in terms of reconstruction quality. The reconstruction results are even much better than for full data using quadratic Tikhonov regularization. All sampling schemes yields comparable performance; however the regular subsampling scheme slightly outperforms the random activation schemes.

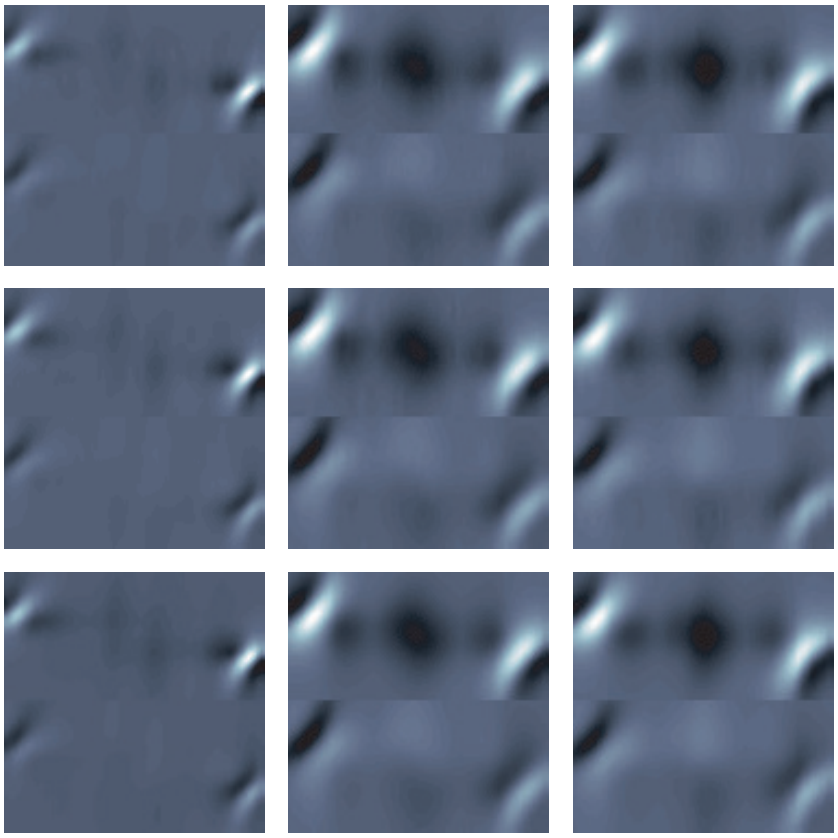

Figure 6: **Reconstructed full data.** The full data **B** have been recovered with Algorithm 2 from the CS data shown in Fig. 5. Top row: Gaussian activation matrix. Middle row: Bernoulli activation matrix. Bottom row: Deterministic activation. The data corresponds to the phantoms shown in Fig. 4 in the same order from left to right.

To further explore the capabilities of Algorithm 1 we also perform experiments using different numbers of CS measurements. For that purpose we repeated the above simulations for $m = 72, 21, 9, 6$ coils activations using the same parameters for image reconstruction. The results are shown in 9. One observes that for the CS-phantom and the tumor-phantom, accurate results are obtained even for very few coil activations. For the more complex Smiley-phantom, the quality significantly decreases with decreasing number of measurements.

Finally, Figure 10 compares the reconstruction results for a small number of $m = 10$ activation patterns. The relative mean squared errors are $(0.58, 0.58, 0.47)$ for the CS-phantom, $(0.38, 0.338, 0.41)$ for the Smiley-phantom and $(0.16, 0.16, 0.17)$ for the Tumor-phantom. While the average reconstruction quality for the CS-phantom over the the whole region of interest is the best for the deterministic sampling scheme, some aspects might be better recovered with the random sampling schemes. For the other two phantoms the random schemes now outperform the Deterministic activation pattern schemes.

4.4 Discussion

Our results clearly demonstrate, that the single-stage approach yields significantly better results than the two-stage approach. While the full measurement data are completed well by Algorithm 2 (see Fig. 6) in the first step of the two-stage approach, recovering the particle distribution

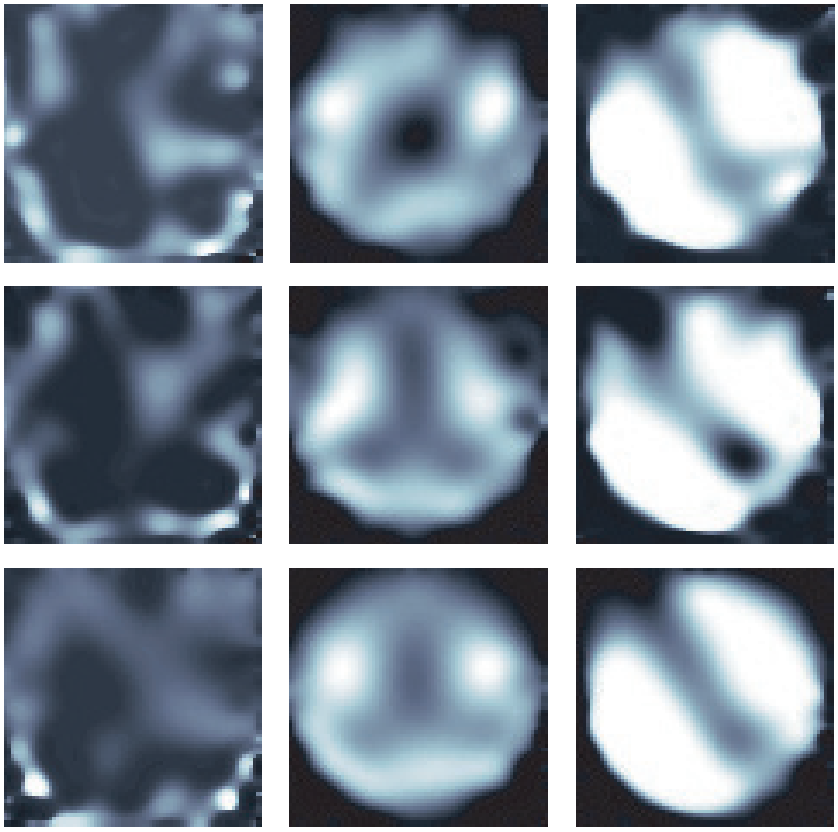

Figure 7: **Results for the two-stage approach.** The magnetic particle distributions have been recovered by applying Algorithm 1 to the completed data shown in Fig. 6 in the same order from left to right. Top row: Gaussian activation matrix. Middle row: Bernoulli activation matrix. Bottom row: Deterministic activation pattern.

using Algorithm 1, performs much better with the original CS data than with the recovered full measurement. One the one hand, this indicates that the data contains key features allowing high quality reconstruction of the magnetic particle distributions. On the other hand, the data completion procedure seemingly fails to recover these key features in a sufficient manner.

For a large numbers of coil activations shown in Fig. 7 and Fig. 8, the deterministic subsampling scheme leads to better results than the random activation. We address this due to the strong smoothing effect of the forward operator, which removes most high frequency components in the data. The regular sparse sampling pattern might therefore yield to the largest information gain given a certain number of linear measurements. For the small number of coil activations shown (see Fig. 10), the random sampling patterns outperforms the deterministic scheme for the Smiley-phantom and the tumor-phantom.

We point out, that hardly any recovery results for compressed sensing applied to severely ill-conditioned matrices $\mathcal{L}$ are available, as $\mathcal{A}\mathcal{L}$ cannot be expected to satisfy the RIP or a similar uniform sparse recovery condition. The numerical results presented in the paper indicate that for the type of considered phantoms (especially the CS-shaped and the tumor-shaped phantom) stable recovery is possible from a small number of coil activations. One might derive such estimates using the recovery result of individual vectors (see Remark 1). Such investigations are an interesting line of future research.

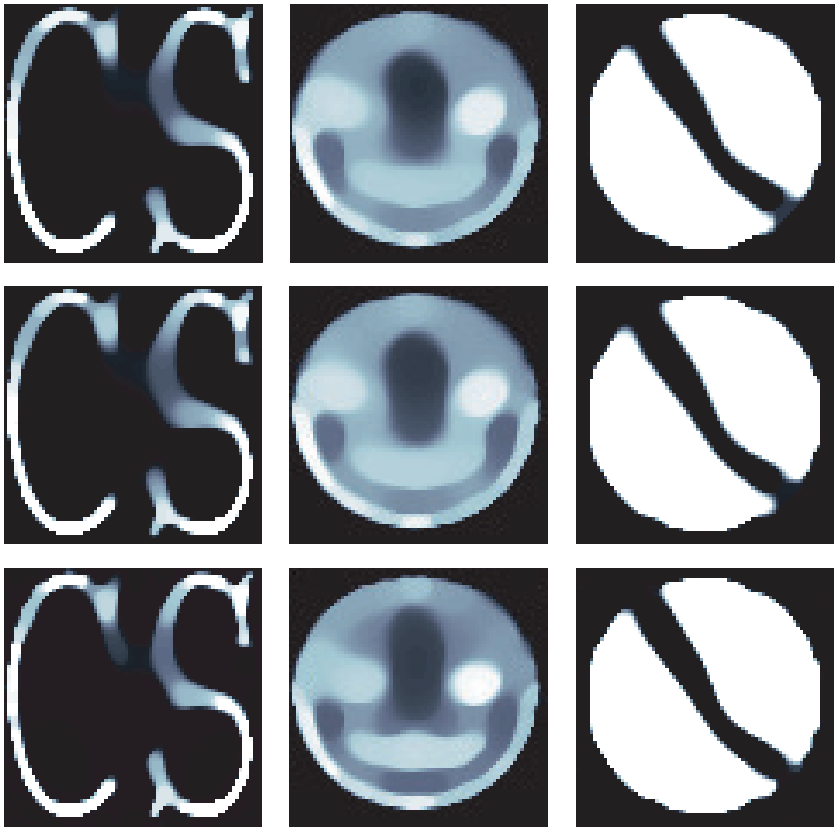

Figure 8: **Results with the single-stage approach.** Data in Fig. 5 is used to directly recover the magnetic particles using Algorithm 1. Top row: Gaussian activation matrix. Middle row: Bernoulli activation matrix. Bottom row: Deterministic activation pattern.

5 Conclusion

The use of multiple coil activation patterns in magnetorelaxometry imaging is time consuming and requires performing several consecutive measurements. It is therefore desirable to make the number of coils activations as small as possible, while keeping high spatial resolution. For that purpose we investigated CS strategies in this paper. We compared Gaussian random activation, Bernoulli activations and deterministic subsampling schemes. Further, we established and compared single-stage and two-stage reconstruction approaches. In the two-stage approach, the full activation data is computed as an intermediate result, whereas in the single stage approach, the magnetic particle distributions is directly recovered from the CS data.

Some conclusions that can be drawn from our numerical experiments are as follows. First, the single-stage approach significantly outperforms the two-stage approach. We therefore propose to use the single-stage approach for ME-MRX image reconstruction. Second, in the experiments with a large number of activations, the deterministic sampling scheme performed better than the random sampling patterns. For a small number of coil activations (see Fig. 8) the random schemes outperform the deterministic scheme for the Smiley-phantom and tumor phantom. Finally, for simple phantoms, a small number of activation patterns seem to be sufficient for accurately estimating the magnetic particle distribution. For actual image reconstruction, we developed an algorithm based on Douglas Rachford splitting. The single-stage algorithm includes a TV penalty as well as accounts for positivity and other known prior. The algorithm performs well for the

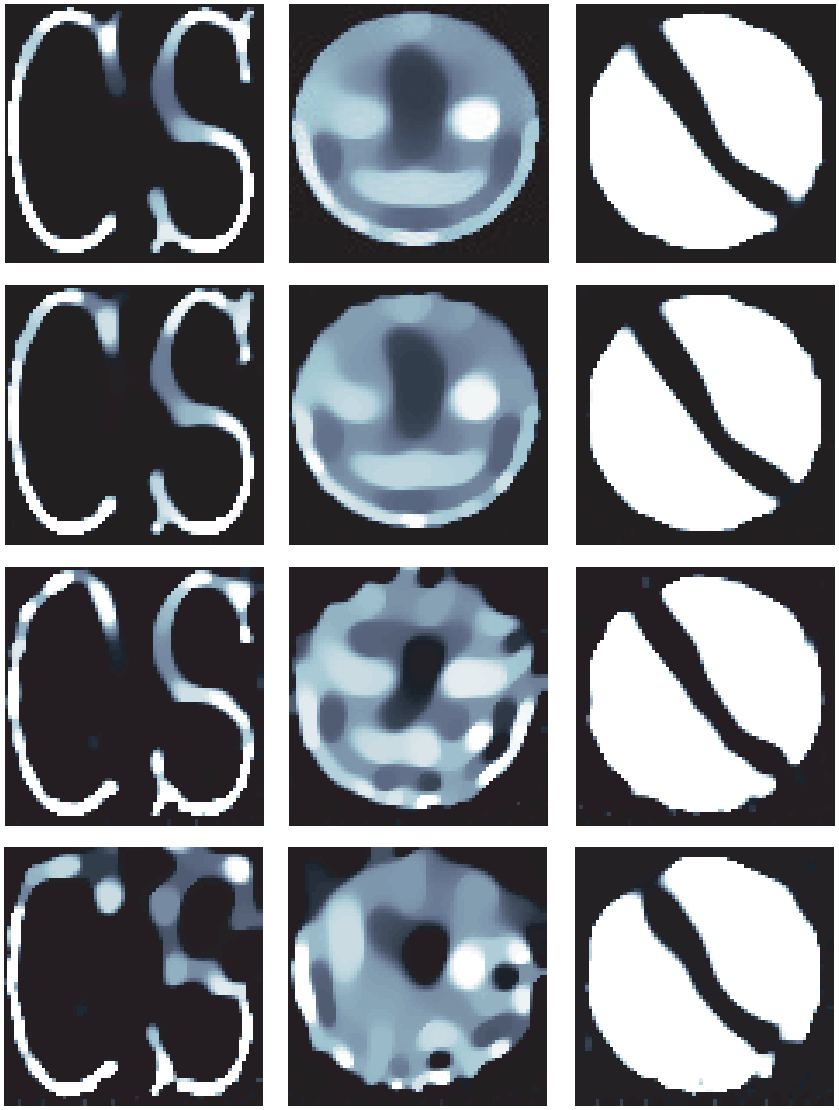

Figure 9: **Reconstruction from different numbers of coil activations.** The particle distribution is recovered with Algorithm 1 using the Deterministic activation pattern scheme with $m = 72, 21, 9, 6$ (from top to bottom) coil activations.

considered setup and recovers the particle distribution in less that one minute on a standard Mac Book (2016).

Several interesting research directions following this work are possible. First, we can replace the inner TV minimization in the single-stage approach by a different algorithm which should accelerate Algorithm 1. Second, the derivation of theoretical error estimates for the single-stage approach is of significant interest. Results in that direction can advice which type of MRX measurements are best to obtain accurate results for certain phantom classes. Moreover, the derivation of adaptive compressed sensing strategies for online monitoring is of significant interest. Advising optimal coil activations given previous activations is a difficult problem that will benefit from theoretical error estimates, numerical simulations as well as a real-world experiments that are currently been implemented. In this paper we investigated standard random compressed sensing schemes (using Gaussian and Bernoulli activation patterns). Using more problem adapted and task oriented measurement design we will expect to derive improved coil activation schemes.

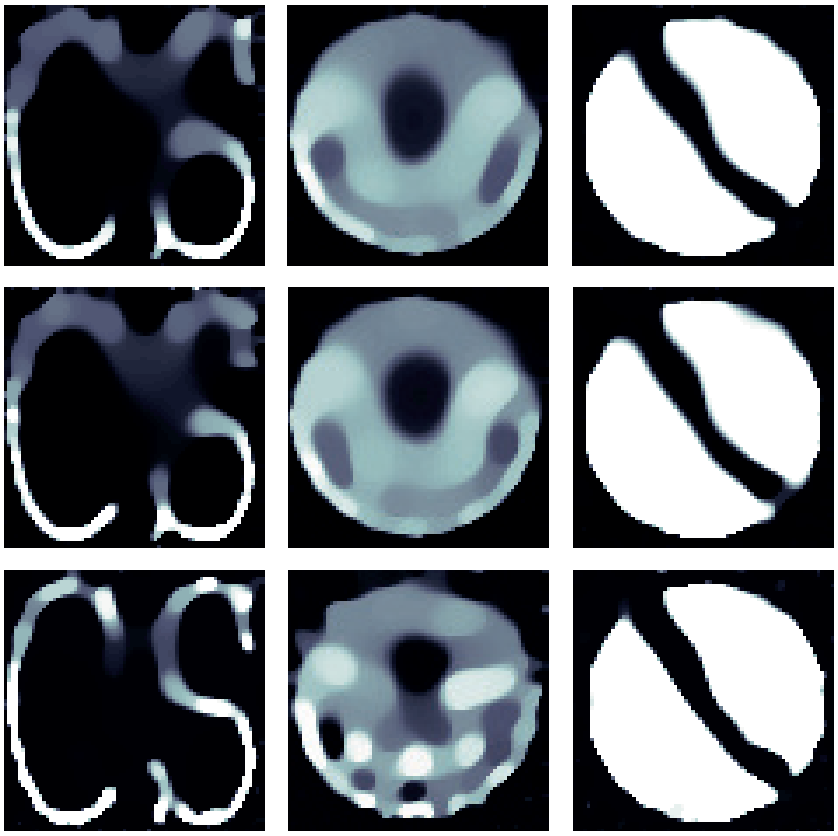

Figure 10: **Comparison of the activation patterns for 10 coil activations.** Reconstruction with the single-stage approach using different activation patterns. Top row: Gaussian activation matrix. Middle row: Bernoulli activation matrix. Bottom row: Deterministic activation pattern.

Acknowledgment

This work has been supported by the Austrian Science Fund (FWF), project P 30747-N32, and the German Science Foundation (DFG) within the priority program COSIP, project Cos-MRXI (BA 4858/2-1).

References

[1] D. Baumgarten, F. Braune, E. Supriyanto, and J. Haueisen. Plane-wise sensitivity based inhomogeneous excitation fields for magnetorelaxometry imaging of magnetic nanoparticles. *J. Magn. Magn. Mater.*, 380:255–260, 2015.

[2] D. Baumgarten, R. Eichardt, G. Crevecoeur, E. Supriyanto, and J. Haueisen. Magnetic nanoparticle imaging by random and maximum length sequences of inhomogeneous activation fields. In *EMBC*, pages 3258–3260, 2013.

[3] D. Baumgarten and J. Haueisen. A spatio-temporal approach for the solution of the inverse problem in the reconstruction of magnetic nanoparticle distributions. *IEEE Trans. Magn.*, 46(8):3496–3499, 2010.

[4] D. Baumgarten, M. Liehr, F. Wiekhorst, U. Steinhoff, P. Münster, P. Miethe, L. Trahms, and J. Haueisen. Magnetic nanoparticle imaging by means of minimum norm estimates from remanence measurements. *Med. Biol. Eng. Comput.*, 46(12):1177–1185, 2008.

[5] E. J. Candès, J. K. Romberg, and T. Tao. Stable signal recovery from incomplete and inaccurate measurements. *Comm. Pure Appl. Math.*, 59(8):1207–1223, 2006.

[6] G.-H. Chen, J. Tang, and S. Leng. Prior image constrained compressed sensing (piccs): a method to accurately reconstruct dynamic ct images from highly undersampled projection data sets. *Med. Phys.*, 35(2):660–663, 2008.

[7] A. Coene, G. Crevecoeur, and L. Dupre. Adaptive control of excitation coil arrays for targeted magnetic nanoparticle reconstruction using magnetorelaxometry. *IEEE Trans. Magn.*, 48(11):2842–2845, 2012.

[8] A Coene, G Crevecoeur, J Leliaert, L Dupré, and G Crevecoeur. Quantitative model selection for enhanced magnetic nanoparticle imaging in magnetorelaxometry. *Med. Phys.*, 42(12):6853, 2015.

[9] A. Coene, J. Leliaert, M. Liebl, N. Loewa, U. Steinhoff, G. Crevecoeur, L. Dupré, and F. Wiekhorst. Multi-color magnetic nanoparticle imaging using magnetorelaxometry. *Phys. Med. Biol.*, 62(8):3139, 2017.

[10] P. L. Combettes and J.-C. Pesquet. Proximal splitting methods in signal processing. In *Fixed-point algorithms for inverse problems in science and engineering*, pages 185–212. Springer, 2011.

[11] D. L. Donoho. Compressed sensing. *IEEE Trans. Inf. Theory*, 52(4):1289–1306, 2006.

[12] Janic Föcke, Daniel Baumgarten, and Martin Burger. The inverse problem of magnetorelaxometry imaging, 2018. arXiv:1802.05937.

[13] S. Foucart and H. Rauhut. *A mathematical introduction to compressive sensing*. Birkhäuser Basel, 2013.

[14] J. J. Fuchs. Recovery of exact sparse representations in the presence of bounded noise. *IEEE Trans. Inf. Theory*, 51(10):3601–3608, 2005.

[15] M. Grasmair, M. Haltmeier, and O. Scherzer. Necessary and sufficient conditions for linear convergence of ℓ^1-regularization. *Comm. Pure Appl. Math.*, 64(2):161–182, 2011.

[16] M. Haltmeier. Stable signal reconstruction via ℓ^1-minimization in redundant, non-tight frames. *IEEE Trans. Signal Process.*, 61(2):420–426, 2013.

[17] M. Haltmeier, T. Berer, S. Moon, and P. Burgholzer. Compressed sensing and sparsity in photoacoustic tomography. *J. Opt.*, 18(11):114004–12pp, 2016.

[18] J. D. Hanson and S. P. Hirshman. Compact expressions for the biot–savart fields of a filamentary segment. *Phys. Plasmas*, 9(10):4410–4412, 2002.

[19] M Liebl, U Steinhoff, F Wiekhorst, J Haueisen, and L Trahms. Quantitative imaging of magnetic nanoparticles by magnetorelaxometry with multiple excitation coils. *Phys. Med. Biol.*, 59(21):6607, 2014.

[20] M. Liebl, F. Wiekhorst, D. Eberbeck, P. Radon, D. Gutkelch, D. Baumgarten, U. Steinhoff, and L. Trahms. Magnetorelaxometry procedures for quantitative imaging and characterization of magnetic nanoparticles in biomedical applications. *Biomed. Tech.*, 60(5):427–443, 2015.

[21] M. Lustig, D. L. Donoho, J. M. Santos, and J. M. Pauly. Compressed sensing mri. *IEEE Sig. Proc. Mag.*, 25(2):72–82, 2008.

[22] H. Richter, M. Kettering, F. Wiekhorst, U. Steinhoff, I. Hilger, and L. Trahms. Magnetorelaxometry for localization and quantification of magnetic nanoparticles for thermal ablation studies. *Phys. Med. Biol.*, 55(3):623–633, 2010.

[23] O. Scherzer, M. Grasmair, H. Grossauer, M. Haltmeier, and F. Lenzen. *Variational methods in imaging*, volume 167 of *Applied Mathematical Sciences*. Springer, New York, 2009.

[24] U. Steinhoff, F. Wiekhorst, D. Baumgarten, J. Haueisen, and L. Trahms. Imaging of magnetic nanoparticles based on magnetorelaxometry with sequential activation of inhomogeneous magnetization fields. *Biomed. Tech.*, 55:22–25, 2010.

[25] B. F. Svaiter. On weak convergence of the Douglas–Rachford method. *SIAM J. Control Optim.*, 49(1):280–287, 2011.

[26] F. Wiekhorst, C. Seliger, R. Jurgons, U. Steinhoff, D. Eberbeck, L. Trahms, and C. Alexiou. Quantification of magnetic nanoparticles by magnetorelaxometry and comparison to histology after magnetic drug targeting. *J. Nanosci. Nanotechnol.*, 6(9-10):3222–3225, 2006.

[27] F. Wiekhorst, U. Steinhoff, D. Eberbeck, and L. Trahms. Magnetorelaxometry assisting biomedical applications of magnetic nanoparticles. *ĂŐPharm. Res.*, 29(5):1189–1202, 2012.